Received: 8 October 2024 | Revised: 7 February 2025 | Accepted: 19 February 2025

DOI: 10.1002/mp.17741

RESEARCH ARTICLE

MEDICAL PHYSICS

Flexible and modular PET: Evaluating the potential of TOF-DOI panel detectors

Gašper Razdevšek[1] | **Georges El Fakhri**[2] | **Thibault Marin**[2] | **Rok Dolenec**[1,3] | **Matic Orehar**[3] | **Yanis Chemli**[2] | **Alberto Giacomo Gola**[4] | **David Gascon**[5] | **Stan Majewski**[6] | **Rok Pestotnik**[1]

[1]Experimental Particle Physics Department (F9), Jožef Stefan Institute, Ljubljana, Slovenia

[2]Yale PET Center, Yale University School of Medicine, New Haven, Connecticut, USA

[3]Faculty of Mathematics and Physics, University of Ljubljana, Ljubljana, Slovenia

[4]Custom Radiation Sensors (CRS), Fondazione Bruno Kessler, Trento, Italy

[5]Institute of Cosmos Sciences (ICCUB), University of Barcelona, Barcelona, Spain

[6]Biomedical Engineering, University of California Davis, Davis, USA

Correspondence
Gašper Razdevšek, Experimental Particle Physics Department (F9), Jožef Stefan Institute, Ljubljana, Slovenia.
Email: gasper.razdevsek@ijs.si

Gašper Razdevšek and Georges El Fakhri both authors contributed equally to this work.

Funding information
HORIZON EUROPE European Research Council, Grant/Award Number: 101099896; Slovenian Research and Innovation Agency, Grant/Award Numbers: BI-US/22-24-165, P1-0389, P1-0135

Abstract

Background: Panel detectors have the potential to provide a flexible, modular approach to Positron Emission Tomography (PET), enabling customization to meet patient-specific needs and scan objectives. The panel design allows detectors to be positioned close to the patient, aiming to enhance sensitivity and spatial resolution through improved geometric coverage and reduced non-collinearity blurring. Parallax error can be mitigated using depth of interaction (DOI) information.

Purpose: One of the key questions the article addresses is: Do panel detectors offer viable clinical imaging capabilities, or does limited angular sampling restrict their utility by causing image distortions and artifacts? Additionally, this article explores the scalability of panel detectors for constructing scanners with a long axial field of view (LAFOV).

Methods: Monte Carlo simulations using GATE software were used to assess the performance of panel detectors with various DOI resolutions and Time-of-Flight (TOF) resolutions as fine as 70 ps. The 30 × 30 cm panels comprised pixelated 3 × 3 × 20 mm LSO crystals. Simulations were run on large high-performance computing clusters (122,000 CPU cores). Open-source CASToR software was used for (TOF MLEM) image reconstruction. The image quality of the scanners was assessed using a range of phantoms (NEMA, Derenzo, XCAT, and a high-resolution brain phantom). The Siemens Biograph Vision PET/CT scanner served as the reference model. The performance of larger 120 × 60 cm panels was also evaluated.

Results: Sensitivity increases over threefold when panel-panel distance is reduced from 80 to 40 cm. The noise equivalent count rate, unmodified by TOF gain, of the panel detectors matches that of the reference clinical scanner at a distance of approximately 50 cm between the panels. Spatial resolution perpendicular to the panels improves from 8.7 to 1.6 mm when the panel-panel distance is reduced, and 70 ps + DOI detectors are used instead of 200 ps, no-DOI detectors. With enhanced TOF and DOI capabilities, panel detectors achieve image quality that matches or surpasses the reference scanner while using about four times less detector material. These detectors can be extended for LAFOV imaging without distortions or artifacts. Additionally, improving TOF and DOI performance enhances contrast-to-noise ratios, thereby improving lesion detection.

Conclusions: A compact 2-panel PET scanner can match the performance of conventional scanners, producing high-quality, distortion-free images. Its mobility and flexibility enable novel applications, including bedside imaging and intensive care unitdiagnostics, as well as imaging in positions such as sitting or standing. Furthermore, the modularity of panel detectors offers the potential to construct cost-effective, high-performance total-body imaging systems.

KEYWORDS
depth of interaction (DOI), GATE Monte Carlo simulations, limited angle pet, panel detectors, time-of-flight (TOF)

1 | INTRODUCTION

Traditional Positron Emission Tomography (PET) scanners, employing a full-ring design, have proven invaluable in clinical diagnosis and research. However, the fixed-radius geometry of ring-based designs inherently limits the flexibility of detector placement for specific applications. This constraint restricts the ability to enhance geometric sensitivity by increasing angular coverage through closer detector placement. We aim to enhance the flexibility of PET systems, tailoring their design to accommodate patient-specific needs and scanning objectives. This approach can potentially replace multiple dedicated scanners with a single, adaptable system.

Our exploration begins with a 2-panel PET system (Figure 1a). Although several studies have investigated 2-panel PET systems, most have used detectors with no or limited time-of-flight (TOF) capabilities. These 2-panel PET systems have been investigated for positron emission mammography[1,2] (no TOF), intraoperative surgical procedures[3] (271 ps TOF), and in-beam PET systems for monitoring proton or heavy ion therapies[4,5] (no TOF). Moreover, large dual flat-panel detectors employing monolithic crystals have been proposed for cost-effective, walk-through total-body PET imaging[6] (predicted 300 ps TOF resolution). Despite their versatility, such 2-panel PET systems often experience reduced resolution in the direction orthogonal to the panels, largely due to insufficient coincidence time resolution (CTR).

In our prior research[7], we validated the critical role of TOF in enhancing sensitivity and improving the spatial resolution of the 2-panel design. However, we also observed a notable decline in spatial resolution when using longer crystals due to parallax error. While shorter crystals reduce parallax error, they significantly reduce sensitivity.

Building on these findings, this study focuses on two main advancements: (1) panel detectors equipped with high-resolution TOF and depth-of-interaction (DOI) capabilities, and (2) large panels (120 × 60 cm) constructed using high-performing modular units. Specifically, the study employs LSO crystals of the standard length of 20 mm, capable of achieving a CTR of approximately 70 ps FWHM. Considering the sub-100 ps FWHM CTR demonstrated using dual-ended crystal readout[8] and our measured CTR of 76 ps[9], our objective of achieving a 70 ps FWHM CTR appears feasible. These advancements pave the way for enhanced sensitivity and resolution in modular, panel-based designs.

In this study, we aim to demonstrate that the combined benefits of high-resolution TOF and DOI capabilities enable practical, high-quality imaging with panel detectors. In addition to compact panels, we explore their modular design to construct long axial field-of-view (LAFOV) scanners, which offer significantly enhanced sensitivity through expanded geometric coverage. This improvement leads to higher-quality images, reduced scanning times, lower tracer dosages, and the potential for delayed imaging beyond multiple tracer half-lives[10]. By demonstrating the clinical utility of smaller panels, we emphasize not only their standalone viability but also their potential to be expanded into larger, more comprehensive systems, aligning with diverse clinical and research requirements.

1.1 | Limited angle PET

2-panel PET systems can be classified into the category of limited angle PET. PET scanners with limited angular coverage generally generate distorted 3D images with artifacts. However, with improved timing resolution of PET detectors, the angular sampling requirement to obtain distortion-free and artifact-free PET images decreases[11,12].

1.2 | TOF

In TOF PET, the high-precision measurement of the difference in the arrival times of the two annihilation photons aids in precisely localizing the emission point along the line-of-response (LOR). This additional information significantly assists in image reconstruction, resulting in reduced noise correlations and an enhanced image signal-to-noise ratio (SNR)[13]. Generally, TOF also makes the reconstruction process more robust and less susceptible to inconsistencies between emission data and various corrections[14]. This is particularly relevant for inconsistent normalization, lack of scatter correction,

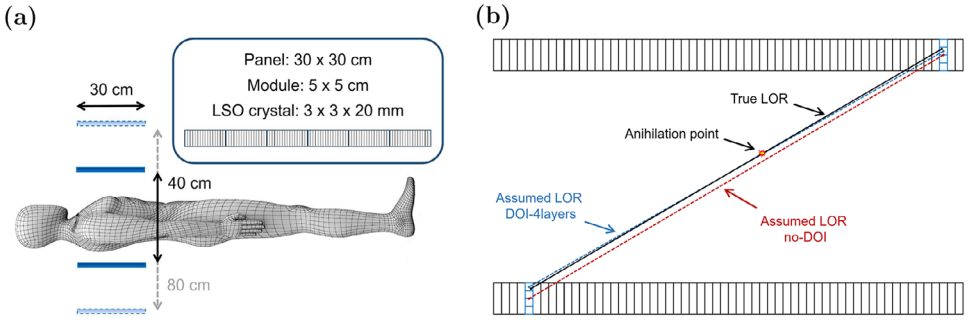

FIGURE 1 (a) A schematic view depicting imaging with 2-panel PET system. While the typical ring diameter of PET scanners is approximately 80 cm, the panel detectors in a flexible system can be brought closer, such as 40 cm, thereby enhancing the sensitivity of the PET system by improving the angular coverage. The figure also shows how the panels are constructed of modules and the size of the LSO crystals. (b) Illustration showing the difference in assumed LOR for a panel detector with and without DOI information. The illustration uses 4-layer DOI encoding to highlight the reduction in parallax error. DOI, depth of interaction; LOR, line-of-response; PET, Positron Emission Tomography.

and mismatched attenuation correction, which can occur in PET/CT during respiratory motion.

Laboratory measurements using a pair of LSO:Ce:Ca crystals coupled to Silicon Photomultipliers (SiPMs) and high-frequency electronics reported a CTR of 58 ± 3 ps for 2 × 2 × 3 mm crystals and 98 ± 3 ps for 2 × 2 × 20 mm crystals[8], whereas top-tier clinical scanners achieve a CTR of approximately 200 ps[15,16], with the latest Siemens clinical model, the Biograph Vision.X, achieving a reported timing resolution of 178 ps[17].

1.3 | DOI

When a 511 keV photon enters the detector at an oblique angle, the varying depth of photon absorption in the scintillator introduces blurring in the spatial point spread function. In clinical whole-body scanners featuring a narrow axial field of view, DOI effects cause minor radial blurring but become a limiting factor for spatial resolution in smaller bore scanners, like preclinical and dedicated organ scanners[18,19]. Consequently, the development of depth-encoding PET detectors in recent years has primarily focused on the high spatial resolution required for preclinical, dedicated breast, and brain PET scanners, and there are currently no whole-body PET scanners with DOI resolution resolution on the market[20,21].

Among the most effective DOI-encoding strategies is placing photodetectors at both the front and back of the scintillator crystal array, known as the dual-ended configuration, which yields DOI resolution as good as 2 mm[22,23]. Most DOI-encoding methods lead to significant scintillation light loss, affecting both energy and timing resolution[24]. However, dual-ended DOI detectors stand out for their ability to maintain excellent timing resolution. Notably, CTR of 98 ± 1 ps FWHM has been demonstrated using 20 mm long LYSO:Ce:Ca crystals in a dual-ended readout configuration[25].

2 | MATERIALS AND METHODS

2.1 | Simulations

This work explores the performance of a 2-panel PET system through Monte Carlo (MC) simulations using GATE software[26] (version 8.2). The comprehensive simulations, totaling more than 100 000 core hours, were executed on the super-computing network [1]. The panel detectors measured 30 × 30 cm, and the spacing between them was adjustable, with a range of panel-panel distances considered, focusing primarily on 40 cm and 80 cm. These detectors comprised LSO crystals, each measuring 3 × 3 × 20 mm. The crystals were organized into modules, each with a 16 × 16 crystal arrangement. A panel detector was constructed using a 6 × 6 arrangement of these modules (Figure 1a). A small gap of 0.01 mm was introduced between the crystals, while the gap between modules was set to 2 mm. The readout was simulated at the module level: signals within each module were summed, and if the total deposited energy was within the specified energy window (Table 1), the event was accepted. The position of the interaction within the module was then determined using an energy centroid approach (GATE *TakeEnergyCentroid*). For coincidence events, all valid coincidence pairs were included (GATE *takeAllGoods* policy). Each coincidence event was characterized by the timing of the first gamma interaction in the first crystal and the first gamma interaction in the second crystal. To simulate the combined effects of optical transfer time spread, photodetector performance (single-photon time resolution), and readout electronics on the timing uncertainty, we added a normally distributed random value to the interaction times. The width of this normal distribution was adjusted to achieve the target CTR between detector pairs for a point source at the center, based on 10 million collected coincidence events.

[1] https://en-vegadocs.vega.izum.si/general-spec/

TABLE 1 Specifications of scanners used in the simulation.

	2-panel system	Reference scanner (SiemensBV-MC)
Scintillator	LSO	LSO
Crystal size	3 x 3 x 20 mm	3.2 x 3.2 x 20 mm
Geometry	Panel: 30 x 30 cm	Ring, diameter: 78 cm
Axial field of view	30 cm	26.3 cm
Energy resolution	10%	10%
Energy window	435 - 585 keV	435 - 585 keV
Coincidence time resolution	200 ps, 70 ps	214 ps
Coincidence time window	2 ns	4.7 ns

For performance comparison, we used the previously constructed Siemens Biograph Vision model, which we have evaluated and confirmed to have good agreement with measured data in terms of noise equivalent count rate (NECR), contrast recovery coefficient, and background variability[27]. The simulated data from this reference model are referred to as *SiemensBV-MC* throughout the article. The energy resolution of the panel detectors was set to 10%, matching that of the reference scanner, and a 435–585 keV energy window was used for all scanners. Table 1 outlines the basic specifications of the simulated scanners.

We used *emstandard_opt4* physics list from Geant4[28], which uses accurate standard and low-energy models of electro-magnetic interactions, making it suitable for medical physics applications[29]. The sources were simulated as back-to-back gamma sources, with the FWHM of the non-collinearity set to 0.5°. The intrinsic detector and acquisition dead times were not taken into account. This can be justified by the fact that the dead time of modern PET scanners is very low compared to traditional PMT-based systems due to minimal or no multiplexing. Therefore, any differences in count rate performance, at least in the range of activities used for clinical imaging, are primarily determined by the system sensitivity[30].

Panel detectors were evaluated with CTRs of 70 ps and 200 ps, while the reference scanner had a CTR of 214 ps. All scanners shared an identical signal processing chain, and they differed only in their DOI capability.

2.2 | Image reconstruction

Only true coincidences were considered in the reconstructions. This way, scatter and random event correction algorithms did not influence our initial performance assessment. We applied the same reconstruction protocols for both the studied 2-panel systems and the SiemensBV-MC using the open-source CASToR software[31] (version 3.1) for iterative 3D TOF MLEM reconstructions. The data from the simulations was obtained in a list-mode format, and a distance-driven projector, based on computations of the overlap between a pair of detector elements and voxels, was used in the reconstructions. The sensitivity image used for image normalization was computed by CASToR. For the sensitivity computation, a loop over the scanner elements was performed, assuming uniform efficiency and no compression, and a true attenuation image containing attenuation coefficients was provided to incorporate attenuation correction into the sensitivity image calculation.

2.3 | DOI implementation

The simulated panel detectors were assumed to incorporate DOI information, a feature practically achievable through methods such as dual-ended readout systems, as discussed in the introduction. Various levels of DOI quality were considered, affecting the number of layers into which the crystal was segmented. Higher DOI resolution allows for more precise discrimination of gamma photon interaction depths within the crystal[20]. The investigated designs comprised 2-layer, 4-layer, 8-layer, and 16-layer DOI configurations using 20 mm long crystals. For example, with a 4-layer segmentation (Figure 1b) of a 20 mm crystal–each layer being 5 mm thick–the highest possible DOI resolution is 5 mm. In the simulation, the crystal was segmented into an appropriate number of layers, and the layer assigned in the coincidence event was determined based on the position of the gamma interaction. If multiple interactions occurred within the detector, the position was obtained using an energy-weighted centroid calculation.

2.4 | Sensitivity

The sensitivity of the PET scanner at varying panel-panel distances, specifically 80, 60, and 40 cm, was systematically evaluated in the axial direction using a point source. The source was incrementally moved in discrete steps of 2 cm. At each position, ten million back-to-back gamma emissions were simulated. The sensitivity was then calculated as the ratio between the true event rate and the source emission rate.

2.5 | NECR

Following the NEMA NU 2-2018 standard [2], the phantom used for this study consisted of a simulated line source

[2] https://www.nema.org/standards/view/Performance-Measurements-of-Positron-Emission-Tomographs

of uniform activity inside the 70-cm long polyethylene cylinder with a diameter of 20 cm. NECR was calculated using the formula:

$$\mathrm{NECR} = \frac{T^2}{T + S + R} \quad (1)$$

Here, T, S, and R represent the true, scatter, and random coincidence count rates, respectively. The type of event was accurately known from the simulation.

The performance of the 2-panel systems in terms of NECR was evaluated at different panel distances ranging from 25 to 80 cm in steps of 5 cm, using an activity concentration of 5 kBq/mL. This activity level, which corresponds to 350 MBq for a 70 L volume, represents a good approximation of a typical administered activity for FDG PET imaging[32].

2.6 | Spatial resolution

Spatial resolution was evaluated by imaging a point source positioned 1 cm above the center of the Field of View (FOV), orthogonal to the panel detectors. As in the sensitivity evaluation, ten million back-to-back gamma emissions (with the FWHM of the non-collinearity set to 0.5°) were simulated, resulting in approximately one million detected events. Subsequently, we conducted image reconstruction using a matrix of voxels measuring 0.5 × 0.5 × 0.5 mm. Spatial resolution, quantified in both the x and y directions (with y being orthogonal to the panels), was determined as the FWHM derived from a Gaussian fit applied to the collected data.

To assess the variation in spatial resolution within the FOV, we simulated a Derenzo phantom featuring hot rods. This particular phantom comprised six sets of rods with diameters measuring 5.0, 4.0, 3.5, 3.0, 2.5, and 2.0 mm, with the inter-rod spacing being identical to the rod diameter. Approximately 10^8 coincidences were acquired for each scanner.

2.7 | NEMA image quality

In all the following studies dealing with phantoms based on human-like geometry, the distance between panels was set to 40 cm (Figure 6a). The thorax-shaped phantom with hot spheres from the NEMA standard was used to determine percent contrast and percent background variability. The background activity was set to 5.3 kBq/cm^3 (0.14 μCi/cm^3), and the ratio between the hot spheres and the background was 4:1. True sphere masks served as regions of interest (ROIs) for contrast recovery calculations, with corrections made to account for the partial volume effects (referred to as partial pixel effects in the case of 2D slice analysis, according to the NEMA standard). This was achieved by expanding the matrix of the reconstructed image by a factor of ten and including only voxels whose centers fell within the ROI.

The phantom was positioned in the center of the scanner, and 4-min scans were simulated. The acquired data were reconstructed into an image with dimensions of 225 × 225 × 225, using 1.6 × 1.6 × 1.6 mm voxels. For the design with a 200 ps FWHM CTR, 40 MLEM iterations were used. In contrast, for the 70 ps FWHM CTR, 20 MLEM iterations were used due to faster convergence. To estimate the variance of contrast recovery coefficients and percent background variability, 10 independent 4-min scans were simulated and analyzed.

2.8 | Application example – brain imaging

The study utilized the publicly available high-resolution [18F]FDG brain phantom[33] to explore the relationship between sensitivity and spatial resolution and to evaluate image reconstruction methods within a realistic context. The employed phantom had a high resolution (400 μm voxel size), featured heterogeneity, and simulated the radiotracer uptake across distinct brain regions. The panels were placed at the side of the head. The mean uptake in the brain was set to $\mathrm{SUV}_{\mathrm{mean}} = 5$, informed by Al-Nabhani et al.[34], and the simulated scan time was 8 min. The dimensions of the reconstructed image were 175 × 175 × 175, while the other reconstruction parameters remained the same as those used in the NEMA image quality study.

2.9 | Exploring LAFOV imaging

To assess the potential and scalability of LAFOV imaging, the size of two-panel detectors was expanded to 120 x 60 cm (Figure 2a). Each large panel is equivalent to four small panels in the axial direction and two in the trans-axial direction. The sensitivity and NECR at the center were initially assessed, employing methods previously utilized for small panels. For image quality evaluation, a highly detailed four-dimensional (4D) eXtended CArdiac-Torso (XCAT) phantom[35] was used. The default male voxelized model, cropped at the thighs to approximate a total length of 1 m, was used to ensure complete coverage within the LAFOV scanner (Figure 2a).

The phantom was composed of a 330 × 200 × 90 matrix with 3 × 3 × 3 mm voxels. The attenuation image, utilized for attenuation correction during image reconstruction, is shown in Figure 2b, and the material map incorporating 18 different materials defined by density and elemental composition is shown in Figure 2c. The activity ratios between the organs and tissues were set

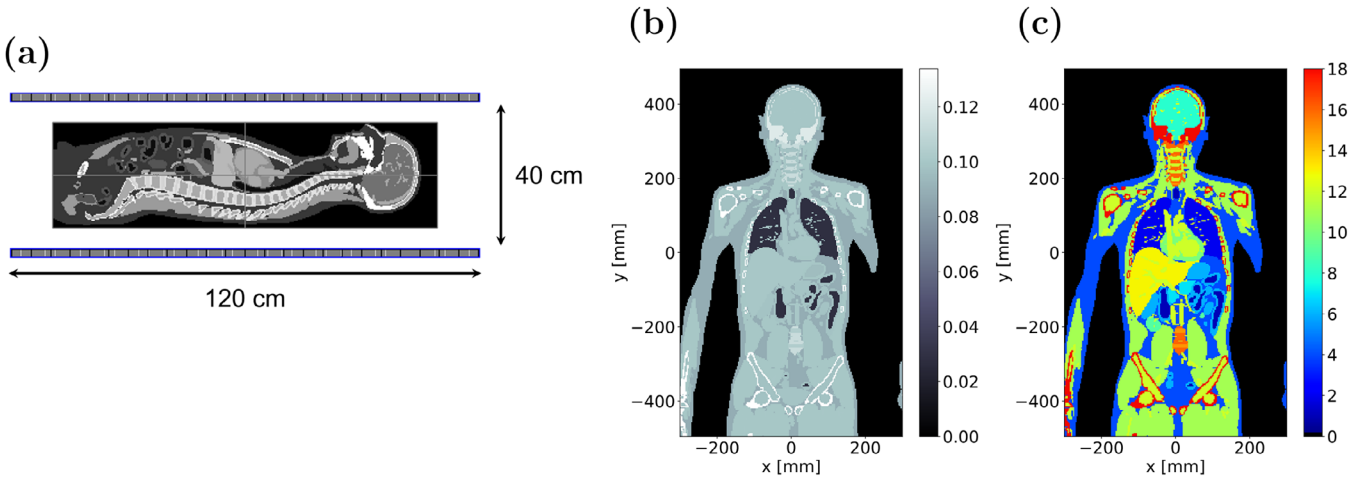

FIGURE 2 (a) Visualization of the GATE simulation using a 1 m long XCAT phantom within a 120 cm long panel system. (b) Attenuation image (cm^{-1}) used for computing the attenuation correction factors. (c) The map of 18 different materials defined in the GATE simulation.

according to the paper by Zincirkeser et al., 2007[36], and following the NEMA standard, the activity of the background (tissues with a standardized uptake value of one) was set to 5.3 kBq/cm^3, resulting in a total inserted activity of approximately 370 MBq (10 mCi).

To evaluate image quality, three nonvoxelized, low-contrast spherical lesions, each 8 mm in diameter, were simulated within the homogeneous regions of the liver, pelvis, and brain areas of the phantom and combined with data from simulations without lesions. The activity of the lesions was set at a 2:1 ratio relative to their background. This setup was designed as an example of a challenging lesion detectability task, particularly for a 200 ps system, rather than as a systematic evaluation of lesion detectability across different sizes and contrasts. The contrast-to-noise ratio (CNR), serving as a surrogate for lesion detectability, was adopted as the metric for image quality[37]. Simulations were conducted to compare two large panel designs: one system with no-DOI and a 200 ps FWHM CTR, and another with an 8-layer DOI and a 70 ps FWHM CTR, utilizing 4 min scans. The 8-layer DOI selection was based on results from the spatial resolution study, which showed no significant difference between the 8-layer DOI and the 16-layer DOI. Additionally, the 8-layer DOI would be easier to achieve and implement in a practical system.

Coincidences were accepted if the maximum axial difference between detected singles events was less than 60 cm (half the panel), corresponding to a maximum acceptance angle of 56.3°. The choice for this maximum axial difference was informed by our study on evaluating axial acceptance effects on scatter fraction and NECR, as discussed in the Appendix A. This acceptance criterion aligns with uEXPLORER data acquisition, where each PET unit can form coincidence events with unit differences up to ±4, for a maximum acceptance angle of 57°[38].

3 | RESULTS

3.1 | Sensitivity

Figure 3a shows the axial sensitivity of both the reference detector and the 2-panel detector at three panel-panel distances: 80, 60, and 40 cm. The sensitivity follows a linear trend with axial position and falls to zero as the axial position reaches ±15 cm, corresponding to the panel's edge. Notably, bringing the panels closer together from 80 to 40 cm yields a significant gain in sensitivity, surpassing a threefold increase. Furthermore, it is noteworthy that the sensitivity achieved with the panels at 40 cm surpasses that of the reference scanner, illustrating the substantial sensitivity improvements achieved by minimizing the panel-panel separation distance.

3.2 | NECR

The study of NECR covered panel-panel distances ranging from 25 to 80 cm. NECR was not modified with TOF gain to evaluate the system based only on the count rate performance. As depicted in Figure 3b, a near-quadratic increase in NECR is observed with reduced panel-panel distance. Notably, the count rate comparable to that of the reference scanner is achieved at approximately 50 cm.

3.3 | Spatial resolution

The scanner's resolution was evaluated using two methods: a point source located near the center and a Derenzo phantom featuring six sets of hot rods with

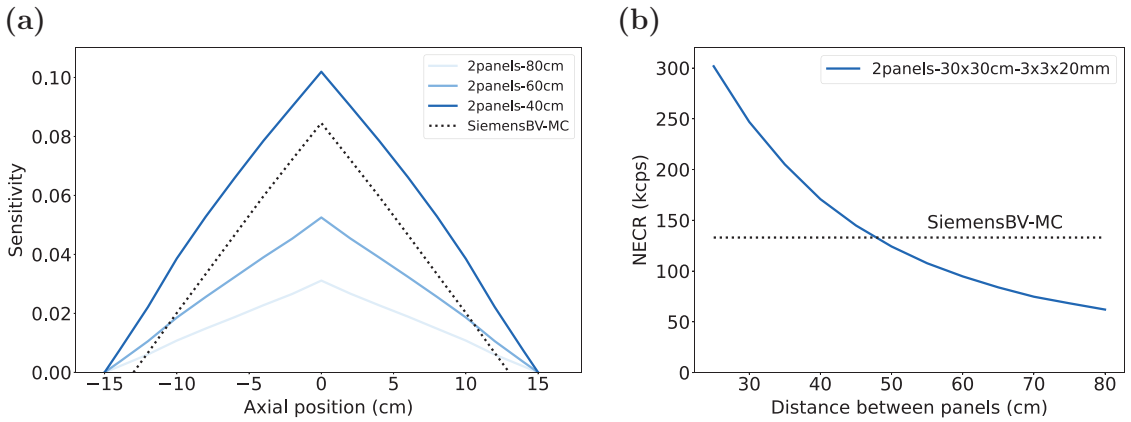

FIGURE 3 (a) Sensitivity in the axial direction for different panel-panel distances. The axial sensitivity of the MC simulated Siemens Biograph Vision is added for reference. (b) NECR dependence of the 2-panel system on the panel-panel distance at an activity concentration of 5 kBq/mL. MC, Monte Carlo; NECR, noise equivalent count rate.

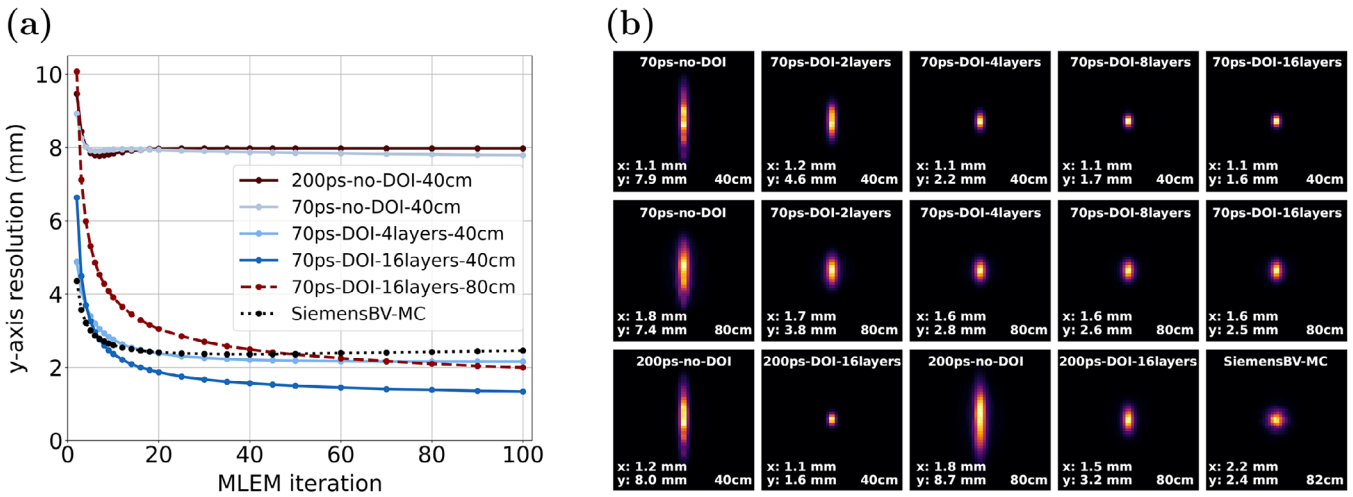

FIGURE 4 (a) Resolution in the *y*-direction (the direction orthogonal to the panels) versus MLEM iterations with varying CTR, DOI resolution, and panel distances. (b) Reconstructed point source images for different panel designs, shown at 40 MLEM iterations. The spatial resolution (FWHM) in the *x* and *y* directions, along with the distance between panels, is noted at the bottom of each image. CTR, coincidence time resolution; DOI, depth of interaction.

diameters ranging from 2 to 5 mm. In Figure 4, both the point source images and the *y*-resolution variation across MLEM iterations are displayed. The images are shown at 40 iterations, which was determined to be close to the convergence point. The elongation of the point source in the direction perpendicular to the panels is clearly visible in the no-DOI design. However, this elongation can be effectively mitigated by incorporating DOI, as the spatial resolution in the y-direction improves from 7.9 to 1.6 mm (Figure 4b). There is a non-significant difference in the spatial resolution between the 8-layer and 16-layer DOI designs. The spatial resolution in the *x*-direction is largely unaffected by DOI resolution variations in this configuration; however, it improves from 1.6 to 1.1 mm as the panel-panel distance is reduced from 80 to 40 cm. Similarly, in the 16-layer DOI design, the *y*-resolution improves from 2.5 to 1.6 mm as the panels are brought closer, from 80 to 40 cm.

Assessing spatial resolution at a singular position within the FOV usually does not fully represent the system's performance at other locations. Therefore, we used a Derenzo phantom to qualitatively evaluate spatial resolution variation across different positions (Figure 5a). Consistent with prior studies, improved timing resolution leads to better spatial resolution, particularly further from the center. As demonstrated in the point source resolution study, utilizing the DOI mitigates parallax error, enabling spatial resolution better than 2.5 mm–that of the reference scanner. This is supported by the line profiles across the reconstructed images (Figure 5b).

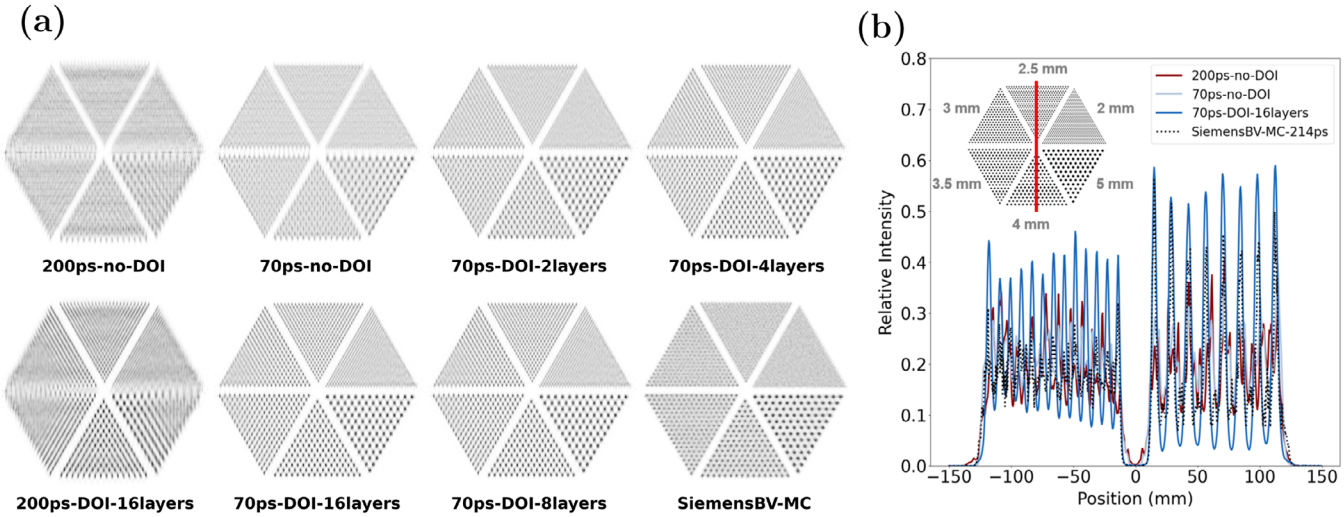

FIGURE 5 (a) Transverse views of the reconstructed images of the Derenzo phantom, where different TOF and DOI are considered. The two panels were placed at the top and bottom. (b) A line profile through the reconstructed Derenzo phantom images, going through the 2.5 and 4 mm diameter rods, with a cross-section of a single voxel, obtained for different detector designs. DOI, depth of interaction; TOF, time-of-flight.

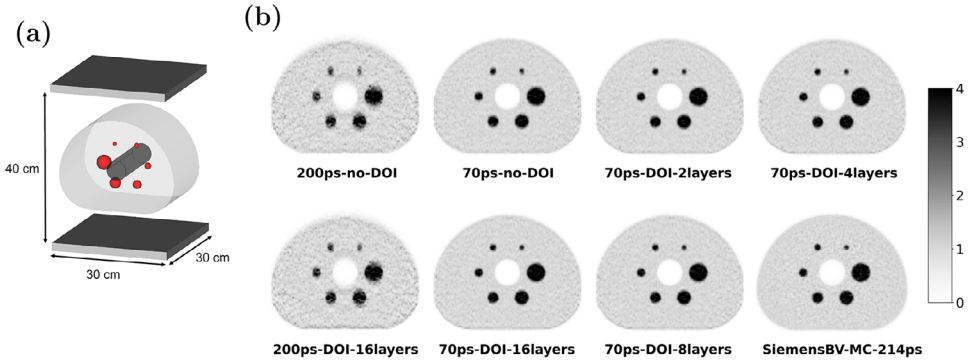

FIGURE 6 (a) A schematic representation of the NEMA image quality phantom positioned within a 2-panel PET system, where the panels are set 40 cm apart. (b) Transverse views of the reconstructed images of the NEMA image quality phantom. PET, Positron Emission Tomography.

3.4 | NEMA image quality

We conducted image reconstructions of the NEMA phantom and subsequently compared the results obtained from panel detectors with varying DOI and TOF capabilities. In Figure 6b, transverse images of the reconstructed phantom are showcased, highlighting the differences in image quality across scanners with distinct performance characteristics. There is a noticeable improvement in image quality as the CTR improves, with further enhancements achieved through the incorporation of DOI information.

To quantitatively assess these improvements, Figure 7 illustrates the relationships between percent contrast and background variability for two hot spheres – 13 mm and 28 mm. These relationships were determined through the analysis of a series of images that underwent Gaussian post-filtering with differing filter widths.

3.5 | Application example – brain imaging

Figure 8 displays reconstructed images of the simulated brain phantom, presenting a realistic context demonstrating how reduced radial elongations, attributed to DOI and TOF information, enhance the level of detail in the reconstructed images. Given the placement of the panels at the sides of the head, these improvements are particularly noticeable in the transverse and coronal slices.

3.6 | Exploring LAFOV imaging

Table 2 shows a table comparing sensitivity, NECR, scatter fraction (SF) and the volume of the crystals, which is a major component of the scanner cost and can be used as a surrogate for the overall scanner

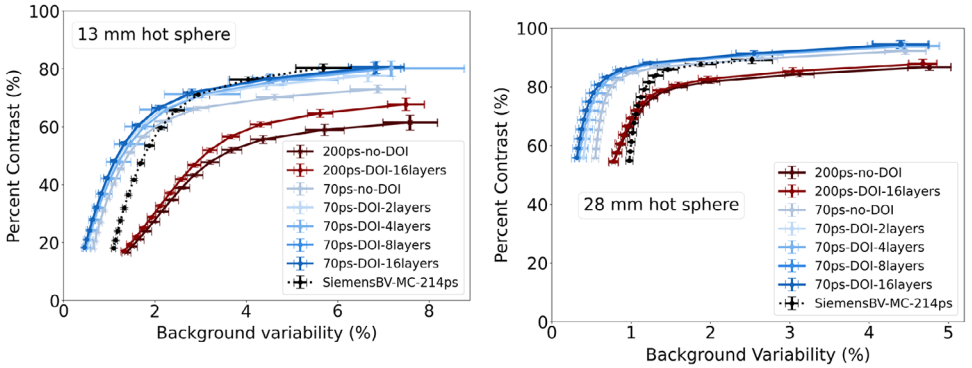

FIGURE 7 Percent contrast versus background variability for a 13 mm and 28 mm diameter hot sphere. Gaussian post-filters with different widths were used to vary the background variability.

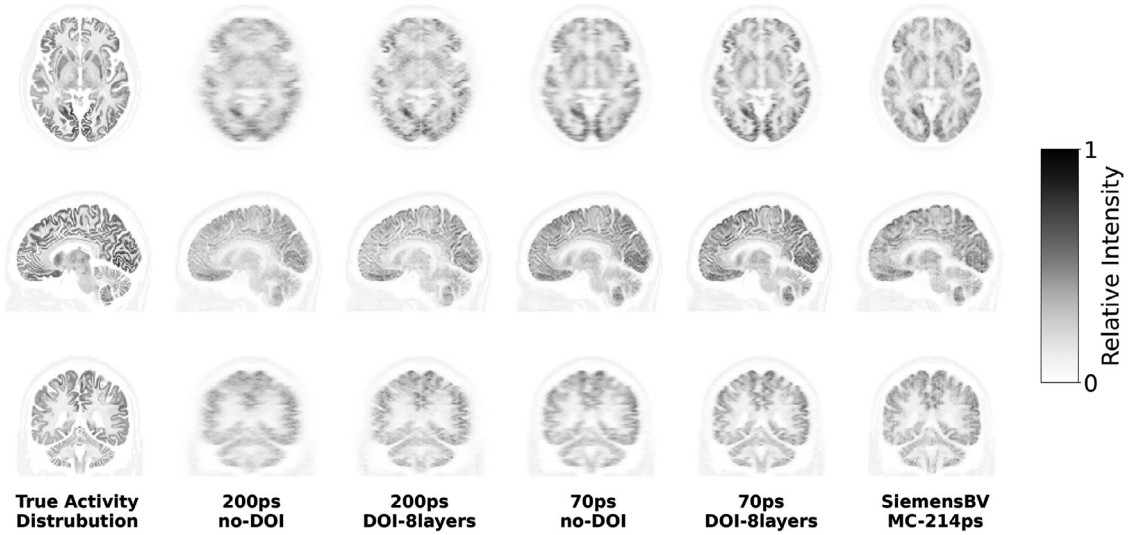

FIGURE 8 Transverse, sagittal, and coronal views of the reconstructed brain images. The first column displays the true activity distribution, which was the input into the MC Simulation. The 8-min simulation yielded 275M true events for the panel scanners and 268M for the SiemensBV. No filtering was applied to the images. MC, Monte Carlo.

TABLE 2 Comparison of sensitivity, NECR, SF, and crystal volume for various designs with a panel-panel distance of 40 cm.

System	Sensitivity	NECR @ 5 kBq/mL (kcps)	SF (%)	Relative crystal volume
SiemensBV-MC	0.085	135	32.5	1
2panels-30x30cm	0.102	171	33.9	0.26
2panels-120x60cm	0.299	1640	34.1	2.1

Abbreviations: NECR, noise equivalent count rate; SF, scatter fraction.

cost. Large panels have approximately 3.5 times higher sensitivity and about 12 times higher NECR compared to the reference scanner while using 2.1 times as much detector material. Figure 9 shows the reconstructed images using an XCAT phantom with inserted hot lesions. The reference scanner is compared also at an equivalent number of true counts, which were obtained in approximately 7 times longer acquisition (28 min). The reconstructed images with large panels using DOI and improved timing show less noise and sharper resolution. In contrast, blurring is observed in the direction perpendicular to the panels in the 200 ps CTR, no-DOI design. This is reflected in the CNR of the inserted lesions (Figure 9). Based on the CNR, the large panel design with 70 ps CTR + DOI demonstrates better lesion detectability compared to the 200 ps CTR, no-DOI design, and the reference scanner.

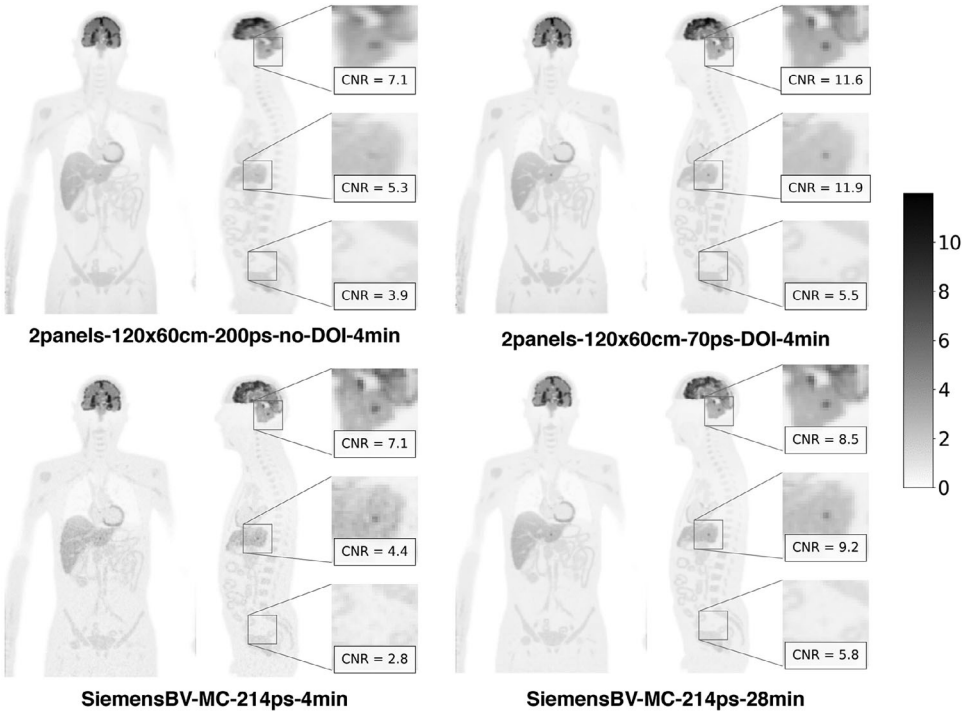

FIGURE 9 Comparison of the reconstructed images of an XCAT phantom with three hot lesions, each 8 mm in diameter, inserted to evaluate their detectability. The acquisition time for the large panels was 4 min (1.74G true events), while the reference scanner images are shown for both the same acquisition time (0.25G events) and for an equivalent count acquisition (28 min). A 5 mm FWHM Gaussian filter was applied to all images.

4 | DISCUSSION

In this study, we evaluated a 2-panel system employing standard-sized LSO crystals with different levels of TOF and DOI capabilities. We also focused on the impact of the panel-panel distance on sensitivity and spatial resolution. The expected increase in sensitivity due to reduced panel-panel distance, resulting from improved angular coverage, aligns with expectations (Figure 3). One of the primary concerns with this unconventional system is spatial resolution and the potential for artifacts. While resolution in the plane parallel to the panels is mainly determined by the crystal face size[39], resolution perpendicular to the panels is significantly influenced by limited angular coverage and parallax error. Although TOF information can compensate for limited angular coverage, it does not address parallax error, which becomes more significant when panels are closer together (Figure 4).

DOI information can effectively mitigate parallax error, and we observed that the performance of scanners with a DOI resolution of 2.5 mm, corresponding to 8-layer segmentation of the 20 mm long crystal, is essentially the same as that of the 16-layer segmentation (Figures 4, 5, and 6b). This observation indicates that, beyond a certain DOI resolution, other factors determining the system's spatial resolution (such as the size of discrete detector elements, blurring due to noncollinearity, positron range, block decoding error, and image reconstruction parameters) begin to dominate. Consequently, even though DOI can theoretically be determined continuously (as with dual-ended readout), the practical gain in spatial resolution is limited compared to discretizing it into a few layers. Discretization also offers benefits in terms of data storage, data transfer rates, and computational efficiency during image reconstruction, as it reduces the complexity of the system matrix and the amount of information that needs to be processed and stored.

The spatial resolution of the point sources was evaluated at 40 MLEM iterations, which was estimated to be close to convergence. Further iterations were avoided, as it is known that the non-negativity constraint of the MLEM algorithm can artificially enhance the apparent spatial resolution, especially when sources are not embedded in a background with suitable relative activity[40].

In the simulations, photon noncollinearity was included, but the positron range was not. For ^{18}F in soft tissue, the positron range introduces an effective blurring of approximately 0.5 mm FWHM[41]. When combined in quadrature with the system's spatial resolution, this results in only a minor degradation, up to 0.1 mm for systems with resolutions above 1 mm ($\sqrt{1^2 + 0.5^2}$ mm = 1.1 mm). However, for isotopes like ^{68}Ga, which emit positrons with higher energy, or in less

dense regions like lung tissue where positrons have longer effective ranges, the impact of positron range on spatial resolution could be more significant.

The contribution of photon non-collinearity to the system spatial resolution can be parameterized by the empirical formula [41]:

$$R_{180^\circ} = 0.0022D \quad (2)$$

where D is the ring diameter of the PET system. For a typical whole-body PET system with $D = 80$ cm, this effect is approximately 1.8 mm. By contrast, for smaller diameters or, in the case of a panel-based system with panel spacing of 40 cm, the contribution is around 0.9 mm. This explains the improved resolution in the x-direction for panel-based designs when the panels are brought closer together (Figure 4), highlighting one of the advantages of a flexible PET system.

Blurring effects, including positron range, can be partially mitigated by incorporating point spread function (PSF) modeling into the reconstruction process. However, PSF modeling was not included in this study to ensure that any observed artifacts could be clearly attributed to limited angular sampling. The development of spatially varying and asymmetric PSF kernels is a promising topic for future studies.

As discussed in the introduction, a DOI resolution of around 2 mm has already been achieved with dual-ended readout. However, achieving a CTR of 70 ps with 20 mm long crystals has yet to be demonstrated. By using the next generation of fast and efficient SiPM photodetectors[9], and by also using DOI information to correct the time estimate of the interaction for the position-of-interaction bias, we believe the 70 ps FWHM CTR is achievable with 20 mm long LSO crystals. However, if detector performance (e.g., CTR) is lower than anticipated, the targeted image quality can still be achieved by using larger panels, which would provide greater sensitivity and enhanced angular sampling. The panel size of 30 × 30 cm was chosen arbitrarily, with the aim of imaging organs such as the brain, prostate, and heart. Optimal panel size may vary depending on the clinical task and can be easily adapted, especially if smaller modules, such as 5 × 5 cm units, are used as versatile building blocks.

Additionally, it should be noted that this excellent CTR with DOI information could also potentially be achieved by other detector designs, such as detectors with lateral side-readout[42] or by using a multi-layer configuration with shorter crystals[43,44]. Detectors using monolithic and semi-monolithic crystals can achieve excellent DOI resolution, and, when combined with decent TOF information[45,46], are also relevant candidates for high-performance panel PET scanners.

The energy resolution of the panel detectors with DOI was assumed to be the same as those without DOI, at 10%. Detectors with dual-ended readout have been demonstrated to achieve such resolutions[47]. Theoretically, given the higher light collection efficiency of dual-ended readout, even greater energy resolution might be achieved using such detectors, which would reduce the scatter fraction and consequently improve the NECR.

With sufficient angular sampling, TOF–at least within the studied range–has little impact on spatial resolution. For instance, the 200ps-DOI-16layers configuration achieves nearly the same spatial resolution as the 70ps-DOI-16layers configuration for a point source near the center when the distance between the panels is 40 cm. In contrast, TOF plays a more significant role in recovering spatial resolution when panels are placed further apart as angular sampling is reduced (Figure 4). For the same reason, it also becomes more important as we move towards the edges of the panels (Figure 5). Therefore, both TOF and DOI are essential for achieving the highest possible spatial resolution within the field of view of limited-angle PET scanners.

Among the configurations evaluated, the 70ps-DOI-16layers design achieves the best resolution. Single-point-source measurements (Figure 4) show that both x and y resolutions are below 2 mm near the center. However, while the 2 mm rods are distinguishable near the center in the Derenzo phantom study, they become progressively harder to distinguish–and eventually indistinguishable–toward the edges (Figure 5).

In addition to improving spatial resolution, TOF also enhances the SNR, as reflected in the percent contrast versus background variability curves (Figure 7). The benefits of combining TOF and DOI are also demonstrated in the brain imaging example (Figure 8).

An important observation from this study is that a two-panel system with a 70 ps FWHM CTR and DOI information can produce images comparable to, if not superior to, top-tier clinical scanners (Figures 6b, and 7) while utilizing four times less detector material (Table 2). This approach offers dual perspectives: maintaining image quality while reducing cost, or improving quality at the same price.

However, achieving DOI capabilities comes with additional trade-offs. DOI achieved with dual-ended readout effectively doubles the number of photodetectors, such as SiPMs, and the associated electronic channels required. This increase demands more advanced data acquisition electronics capable of handling the higher number of channels and data rates, introducing additional cost. While these costs offset some of the material savings offered by panel detectors, the overall system cost may still be lower. Assuming the cost of SiPMs and electronics is roughly equal to that of the scintillator material[48], doubling the cost of SiPMs and electronics while reducing the scintillator cost by a factor of four should still result in a more cost-effective overall system.

Extending axial coverage in a cost-effective manner is another promising advantage of panel detectors. Comparing the large panels with the SiemensBV-MC, the NECR is increased by about a factor of 12, while the amount of crystal material used in the detectors is approximately doubled. The increased sensitivity can be utilized to reduce either the dose or the acquisition time. For instance, in the XCAT study, the acquisition time for the SiemensBV-MC scanner was approximately 7 times longer to obtain an equivalent number of true counts across multiple bed positions.

The benefits seen with smaller panels – like improved CTR and DOI data, leading to enhanced spatial resolution and reduced background noise – are also observed in larger panels, as indicated by the CNR of the lesions (Figure 9). Our results with larger panels indicate that these detectors are scalable and not only capable of producing images without distortions or artifacts but can also detect small, low-contrast lesions with high accuracy.

The reconstructed images in this study are based solely on true coincidences. As a result, the reconstructed images are 'ideal' in the sense that they are free from the noise introduced by correction algorithms. However, the results still allow for a relative performance comparison because, for panel-based scanners, the behavior of the detectors and signal processing chain was modeled after the Siemens Biograph Vision. This modeling includes key parameters such as crystal length, readout, coincidence sorting, energy resolution, and the energy window. As a result, scatter fractions among the compared scanners are very similar, as shown in Table 2, even for the large-panel design. The influence of scatter and random corrections on image quality for large panels was assessed in the Appendix B. The results show that the CNR of the lesions is reduced due to increased noise. However, both panel detectors and the SiemensBV-MC scanner are affected in a similar manner. Assuming the correction is properly implemented–introducing only noise but no bias–images with equivalent noise levels to those reconstructed from only true coincidences could be achieved in approximately T/NECR longer scan time, which for large panels results in about a factor of 1.9.

Panel detectors also enable the construction of mobile systems. We are currently developing a prototype to experimentally verify the predicted performance from simulations. One consideration is that the mobile system will be CT-less, which raises the issue of attenuation and scatter correction. While a CT image can be obtained from a separate scan, this may not always be practical or desirable. A promising feature of TOF PET is that it enables joint reconstruction of activity and attenuation, even when CT-based attenuation images are subject to misalignment or are unavailable[49]. Improved TOF capabilities can further enhance this joint reconstruction process[50]. Another possibility is the use of deep learning-based CT-less attenuation and scatter correction, where a CT image or a fully corrected PET image is estimated directly from non-corrected PET data[51–53]. Optimal reconstruction with panel detectors remains an area of ongoing research.

5 | CONCLUSION

This study demonstrates that a relatively compact 2-panel system can achieve image quality comparable to clinical scanners, free of distortions or artifacts. While TOF is crucial to compensate for limited angular sampling, DOI adds an extra dimension to improving image quality by mitigating parallax error and enhancing spatial resolution beyond that of commercially available whole-body PET scanners. Although state-of-the-art timing resolution of 58 ps was demonstrated with short 3 mm LSO crystals, we anticipate achieving the targeted 70 ps FWHM CTR using standard-length crystals with dual-ended readout, which also offers convenient access to DOI information. Such detectors facilitate novel scanner geometries for clinical use, exemplified by the 2-panel system in this study. Moreover, the possibility of an open geometry–where module placement is not constrained to a ring and allows for incomplete sampling–enables for novel combinations with other imaging modalities, such as MRI, paving the way for integrated and comprehensive diagnostic approaches. The panel detector design's notable advantage lies in its flexibility and modularity, allowing the assembly of cost-effective LAFOV scanners by combining multiple panels. This flexibility, combined with mobility, opens new application avenues, such as imaging in sitting or standing positions, enabling higher comfort during scans and improving accessibility for patients with mobility issues. Additionally, its open geometry provides access to the patient, which is particularly useful for biopsy or particle therapy, as well as imaging in the Intensive Care Units (ICUs). Future work will focus on building and testing the proposed panel scanners, as well as optimizing the reconstruction algorithm for panel detectors. This includes implementing panel-specific PSF modeling and exploring CT-less attenuation and scatter correction methods.

ACKNOWLEDGMENTS

This work was supported by the European Union's Horizon Europe research and innovation programme under grant agreement No. 101099896, and from Slovenian Research and Innovation Agency grants No. BI-US/22-24-165, P1-0389 and P1-0135.

CONFLICT OF INTEREST STATEMENT

The authors declare no conflicts of interest.

REFERENCES

1. MacDonald L, Edwards J, Lewellen T, Haseley D, Rogers J, Kinahan P. Clinical imaging characteristics of the positron emission mammography camera: PEM Flex Solo II. *J Nucl Me*. 2009;50(10):1666-1675. doi: 10.2967/jnumed.109.064345
2. Shi Y, Wang Y, Zhou J, et al. DH-Mammo PET: a dual-head positron emission mammography system for breast imaging. *Phys Med Biol*. 2022;67(20):205004. doi: 10.1088/1361-6560/ac934c
3. Sajedi S, Bläckberg L, Majewski S, Sabet H. Limited-angle TOF-PET for intraoperative surgical applications: proof of concept and first experimental data. *JINST*. 2022;17(01):T01002. doi: 10.1088/1748-0221/17/01/T01002
4. Ferrero V, Fiorina E, Morrocchi M, et al. Online proton therapy monitoring: clinical test of a silicon-photodetector-based in-beam PET. *Sci Rep*. 2018;8(1):4100. doi: 10.1038/s41598-018-22325-6
5. Gao M, Chen HH, Chen FH, et al. First results from all-digital PET dual heads for in-beam beam-on proton therapy monitoring. *IEEE Trans Radiat Plasma Med Sci*. 2021;5(6):775-782. doi: 10.1109/TRPMS.2020.3041857
6. Vandenberghe S, Muller F, Withofs N, et al. Walk-through flat panel total-body PET: a patient-centered design for high throughput imaging at lower cost using DOI-capable high-resolution monolithic detectors. *Eur J Nucl Med Mol Imaging*. 2023;50:1-14. doi: 10.1007/s00259-023-06341-x
7. Razdevšek G, Dolenec R, Križan P, et al. Multi-panel limited angle PET system with 50 ps FWHM coincidence time resolution: a simulation study. *IEEE trans radiat plasma med sci*. 2022;6(6):721-730. doi: 10.1109/TRPMS.2021.3115704
8. Gundacker S, Turtos RM, Auffray E, Paganoni M, Lecoq P. High-frequency SiPM readout advances measured coincidence time resolution limits in TOF-PET. *Phys Med Biol*. 2019;64(5):055012. doi: 10.1088/1361-6560/aafd52
9. Mariscal-Castilla A, Gómez S, Manera R, et al. Toward Sub-100 ps TOF-PET systems employing the FastIC ASIC With analog SiPMs. *IEEE Trans Radiat Plasma Med Sci*. 2024;8(7):718-733. doi: 10.1109/TRPMS.2024.3414578
10. Cherry SR, Jones T, Karp JS, Qi J, Moses WW, Badawi RD. Total-body PET: maximizing sensitivity to create new opportunities for clinical research and patient care. *J Nucl Med*. 2018;59(1):3-12. doi: 10.2967/jnumed.116.184028
11. Gravel P, Li Y, Matej S. Effects of TOF resolution models on edge artifacts in PET reconstruction from limited-angle data. *IEEE trans radiat plasma med sci*. 2020;4(5):603-612. doi: 10.1109/TRPMS.2020.2989209
12. Gonzalez-Montoro A, Pavón N, Barberá J, et al. Design and proof of concept of a double-panel TOF-PET system. *EJNMMI Phys*. 2024;11:73. doi: 10.1186/s40658-024-00674-8
13. Surti S. Update on time-of-flight PET imaging. *J Nucl Med*. 2015;56:98-105. doi: 10.2967/jnumed.114.145029
14. Conti M. Why is TOF PET reconstruction a more robust method in the presence of inconsistent data?. *Phys Med Biol*. 2011;56:155-68. doi: 10.1088/0031-9155/56/1/010
15. Sluis vJ, Jong dJ, Schaar J, et al. Performance characteristics of the digital biograph vision PET/CT System. *J Nucl Med*. 2019;60(7):1031-1036. doi: 10.2967/jnumed.118.215418
16. Li G, Ma W, Li X, et al. Performance evaluation of the uMI panorama PET/CT system in accordance with the national electrical manufacturers association NU 2-2018 Standard. *J Nucl Med*. 2024;65(4):652-658. doi: 10.2967/jnumed.123.265929
17. Siemens Healthineers. Biograph Vision.X PET/CT Scanner. Accessed November 2, 2024. www.siemens-healthineers.com/si/molecular-imaging/pet-ct/biograph-vision#Biograph-Vision.X
18. Yoshida E, Yamaya T. PET detectors with depth-of-interaction and time-of-flight capabilities. *Radiol Phys Technol*. 2024;17(3):596-609. doi: 10.1007/s12194-024-00821-x
19. LaBella A, Cao X, Petersen E, et al. High-Resolution depth-encoding pet detector module with prismatoid light-guide array. *J Nucl Med*. 2020;61(10):1528-1533. doi: 10.2967/jnumed.119.239343
20. Liu Z, Niu M, Kuang Z, et al. High resolution detectors for whole-body PET scanners by using dual-ended readout. *EJNMMI Phys*. 2022;9(1):29. doi: 10.1186/s40658-022-00460-4
21. Zeng X, Wang Z, Tan W, et al. A conformal TOF–DOI Prism-PET prototype scanner for high-resolution quantitative neuroimaging. *Med Phys*. 2023;50(6):3401-3417. doi: 10.1002/mp.16223
22. Kuang Z, Wang X, Fu X, et al. Dual-ended readout small animal PET detector by using 0.5 mm pixelated LYSO crystal arrays and SiPMs. *Nucl Instrum Methods Phys Res A*. 2019;917:1-8. doi: 10.1016/j.nima.2018.11.011
23. Du J, Ariño-Estrada G, Bai X, Cherry S. Performance comparison of dual-ended readout depth-encoding pet detectors based on BGO and LYSO crystals. *Phys Med Biol*. 2020;65(23):235030. doi: 10.1088/1361-6560/abc365
24. Berg E, Cherry SR. Innovations in Instrumentation for Positron Emission Tomography. *Semin Nucl Med*. 2018;48(4):311-331. doi: 10.1053/j.semnuclmed.2018.02.006
25. Weindel K, Nadig V, Herweg K, Schulz V, Gundacker S. A time-based double-sided readout concept of 100 mm LYSO:Ce,Ca fibres for future axial TOF-PET. *EJNMMI Phys*. 2023;10:43. doi: 10.1186/s40658-023-00563-6
26. Jan S, et al. GATE: a simulation toolkit for PET and SPECT. *Phys Med Biol*. 2004;49(19):4543-4561. doi: 10.1088/0031-9155/49/19/007
27. Razdevšek G, Pestotnik R, Križan P, et al. Exploring the potential of a cherenkov TOF PET Scanner: a simulation study. *IEEE Trans Radiat Plasma Med Sci*. 2023;7(1):52-61. doi: 10.1109/TRPMS.2022.3202138
28. Agostinelli S, et al. Geant4 - a simulation toolkit. *Nucl Instrum Methods Phys Res A*. 2003;506(3):250-303. doi: 10.1016/S0168-9002(03)01368-8
29. Allison J, et al. Recent developments in Geant4. *Nucl Instrum Methods Phys Res A*. 2016;835:186-225. doi: 10.1016/j.nima.2016.06.125
30. Surti S, Karp JS. Update on latest advances in time-of-flight PET. *Phys Med*. 2020;80:251-258. doi: 10.1016/j.ejmp.2020.10.031
31. Merlin T, Stute S, Benoit D, et al. CASToR: a generic data organization and processing code framework for multi-modal and multi-dimensional tomographic reconstruction. *Phys Med Biol*. 2018;63(18):185005. doi: 10.1088/1361-6560/aadac1
32. Boellaard R, Delgado Bolton RC, Oyen W, et al. FDG PET/CT: EANM procedure guidelines for tumour imaging: version 2.0. *Eur J Nucl Med Mol Imaging*. 2015;42:328–354. doi: 10.1007/s00259-014-2961-x
33. Belzunce MA, Reader AJ. Technical Note: Ultra high-resolution radiotracer-specific digital pet brain phantoms based on the BigBrain atlas. *Med Phys*. 2020;47(8):3356-3362. doi: 10.1002/mp.14218
34. Al-Nabhani KZ, Syed R, Michopoulou S, et al. Qualitative and quantitative comparison of PET/CT and PET/MR imaging in clinical practice. *J Nucl Med*. 2014;55(1):88-94. doi: 10.2967/jnumed.113.123547
35. Segars WP, Tsui BMW, Cai J, Yin FF, Fung GSK, Samei E. Application of the 4D XCAT phantoms in biomedical imaging and beyond. *IEEE Trans Med Imag*. 2018;37(3):680-692. doi: 10.1109/TMI.2017.2738448
36. Zincirkeser S, Şahin E, Halac M, Sager S. Standardized uptake values of normal organs on 18F-Fluorodeoxyglucose positron emission tomography and computed tomography imaging. *J Int Med Res*. 2007;35:231-236. doi: 10.1177/147323000703500207
37. Yan J, Schaefferkoetter J, Conti M, Townsend D. A method to assess image quality for Low-dose PET: Analysis of SNR, CNR,

bias and image noise. *Cancer Imaging*. 2016;16(26):1. doi: 10.1186/s40644-016-0086-0
38. Spencer BA, Berg E, Schmall JP, et al. Performance evaluation of the uEXPLORER total-body PET/CT scanner based on nema nu 2-2018 with additional tests to characterize PET scanners with a long axial field of view. *J Nucl Med*. 2021;62(6):861-870. doi: 10.2967/jnumed.120.250597
39. Orehar M, Dolenec R, El Fakhri G, et al. Design optimisation of a flat-panel, limited-angle TOF-PET scanner: a simulation study. *Diagnostics*. 2024;14(17):1976. doi: 10.3390/diagnostics14171976
40. Gong K, Cherry SR, Qi J. On the assessment of spatial resolution of PET systems with iterative image reconstruction. *Phys Med Biol*. 2016;61(5):N193. doi: 10.1088/0031-9155/61/5/N193
41. Moses WW. Fundamental limits of spatial resolution in PET. *Nucl Instrum Methods Phys Res, Sect A*. 2011;648:S236-S240. doi: 10.1016/j.nima.2010.11.092
42. Lee MS, Cates J, González A, Levin C. High-resolution time-of-flight PET detector with 100 ps coincidence time resolution using a side-coupled phoswich configuration. *Phys Med Biol*. 2021;66:125007. doi: 10.1088/1361-6560/ac01b5
43. Vandenbroucke A, Foudray AMK, Olcott PD, Levin CS. Performance characterization of a new high resolution PET scintillation detector. *Phys Med Biol*. 2010;55(19):5895. doi: 10.1088/0031-9155/55/19/018
44. Consuegra D, Korpar S, Križan P, Pestotnik R, Razdevšek G, Dolenec R. Simulation study to improve the performance of a whole-body PbF2 Cherenkov TOF-PET scanner. *Phys Med Biol*. 2020;65(5):055013. doi: 10.1088/1361-6560/ab6f97
45. Lamprou E, Gonzalez AJ, Sanchez F, Benlloch JM. Exploring TOF capabilities of PET detector blocks based on large monolithic crystals and analog SiPMs. *Phys Med*. 2020;70:10-18. doi: 10.1016/j.ejmp.2019.12.004
46. Mueller F, Naunheim S, Kuhl Y, Schug D, Solf T, Schulz V. A semi-monolithic detector providing intrinsic DOI-encoding and sub-200 ps CRT TOF-capabilities for clinical PET applications. *Med Phys*. 2022;49(12):7469-7488. doi: 10.1002/mp.16015
47. Yang Q, Sang Z, Zhang C, Du J. Performance of two depth-encoding dual-ended readout PET detectors based on SiPM arrays with the same pitch size and different active areas. *JINST*. 2020;15(11):T11003. doi: 10.1088/1748-0221/15/11/T11003
48. Vandenberghe S, Moskal P, Karp J. State of the art in total body PET. *EJNMMI Physics*. 2020;7:35. doi: 10.1186/s40658-020-00290-2
49. Rezaei A, Deroose CM, Vahle T, Boada F, Nuyts J. Joint Reconstruction of Activity and Attenuation in Time-of-Flight PET: A Quantitative Analysis. *J Nucl Med*. 2018;59(10):1630-1635. doi: 10.2967/jnumed.117.204156
50. Hemmati H, Kamali-Asl A, Ghafarian P, Rahmim A, Zaidi H, Ay MR. List-mode quantitative joint reconstruction of activity and attenuation maps in Time-of-Flight PET. *JINST*. 2023;18(09):P09041. doi: 10.1088/1748-0221/18/09/P09041
51. Arabi H, Zaidi H. Deep learning-guided estimation of attenuation correction factors from time-of-flight PET emission data. *Med Image Anal*. 2020;64:101718. doi: 10.1016/j.media.2020.101718
52. Hwang D, Kang S, Kim KY, Choi H, Lee JS. Comparison of deep learning-based emission-only attenuation correction methods for positron emission tomography. *EJNMMI*. 2022;49:1833–1842. doi: 10.1007/s00259-021-05637-0
53. Guo R, Xue S, Hu J, et al. Using domain knowledge for robust and generalizable deep learning-based CT-free PET attenuation and scatter correction. *Nat Commun*. 2022;13:5882. doi: 10.1038/s41467-022-33562-9
54. Tashima H, Akamatsu G, Yamashita T, Yamaya T. Scatter correction with image-domain interpolation for TOF helmet-type PET. In: *2021 IEEE NSS/MIC*, 2021:1-2. doi: 10.1109/NSS/MIC44867.2021.9875785

How to cite this article: Razdevšek G, Fakhri GE, Marin T, et al. Flexible and modular PET: Evaluating the potential of TOF-DOI panel detectors. *Med Phys*. 2025;52:2845–2860. https://doi.org/10.1002/mp.17741

APPENDIX A: EVALUATION OF THE AXIAL ACCEPTANCE EFFECTS ON SCATTER FRACTION AND NECR IN LARGE-PANEL CONFIGURATIONS

Figure A1 shows the impact of NECR and SF on axial acceptance in the large-panel configuration. NECR and SF are evaluated at maximum axial acceptance differences of 10, 20, 40, 60, and 120 cm, corresponding to maximum acceptance angles of 14.0°, 26.6°, 45°, 56.3°, and 71.6°, respectively. The scatter fraction does not vary significantly with increasing axial acceptance, as both true and scatter events scale approximately in the same manner. In contrast, NECR increases and reaches a plateau at about half a panel (60 cm), beyond which random events begin to heavily dominate the detected coincidences. This effect is further influenced by our coincidence sorting policy, which considers all good coincidences.

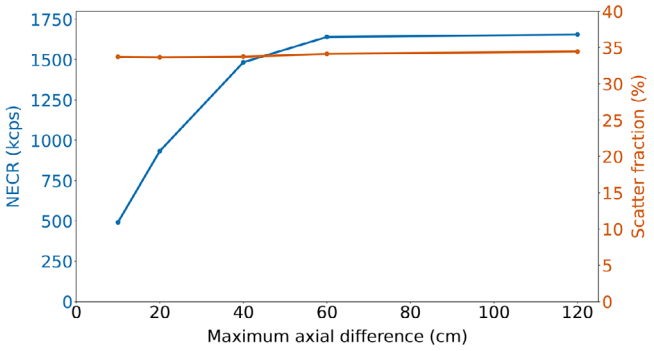

FIGURE A1 NECR and scatter fraction as a function of the maximum axial difference used to accept coincidences. If no axial filtering is applied, the maximum axial difference corresponds to the full length of the large panel (120 cm). NECR, noise equivalent count rate.

APPENDIX B: ASSESSING THE INFLUENCE OF SCATTER AND RANDOM CORRECTIONS ON IMAGE QUALITY

The method used to assess the impact of scatter and random correction on image quality is based on the assumption that the MLEM reconstruction method is linear, allowing different types of coincidences (T: trues, S: scatters, R: randoms) to be reconstructed independently. Although MLEM is generally not a linear algorithm, it exhibits near-linear behavior during the first few tens of

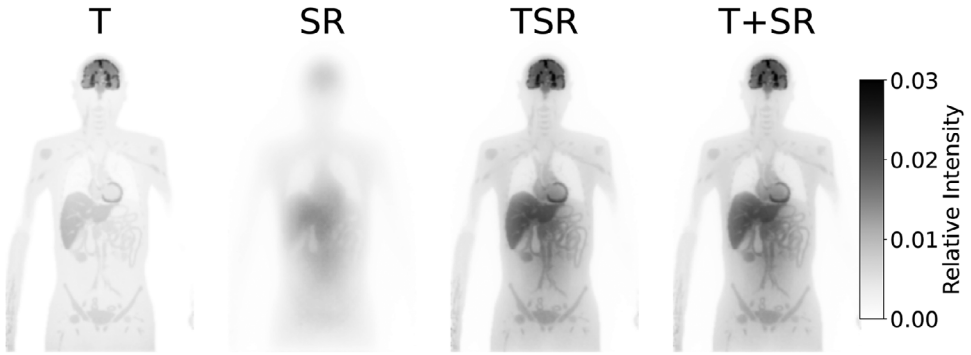

FIGURE B1 Reconstructed images using only trues (T), only scatter and randoms (SR), and all coincidences combined (TSR). The T+SR image is obtained by separately reconstructing the T and SR images and then adding them.

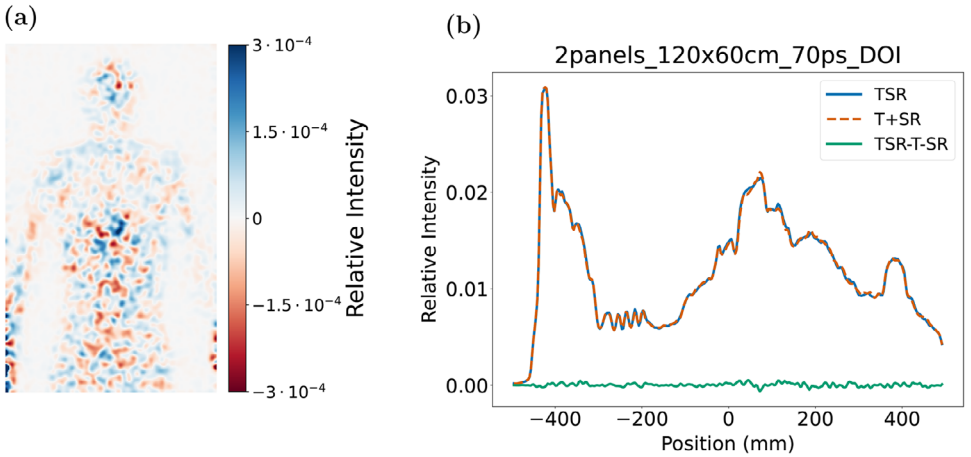

FIGURE B2 (a) Difference image between TSR and T+SR reconstructions for the 2panels_120x60cm_70ps_DOI design. Note that the color bar scale is 100 times smaller than that in Figure B2, indicating that the maximum voxel-level differences are on the order of 1%. (b) Profile through the center of the phantom along the longitudinal axis, comparing TSR, T+SR, and the difference image (TSR – T – SR).

iterations. Previous work conducted on a Siemens Biograph Vision–type scanner geometry demonstrated that this assumption introduces less than 1% error in percent contrast measurements of the NEMA image quality phantom[27]. A similar method, with image-domain interpolation, was implemented for the TOF helmet-type PET, showing improved image contrast compared with the conventional projection-domain method[54].

Here, we test and apply this method to the large-panel configuration. Figure B1 shows reconstructed images from different types of coincidences, and Figure B2 shows the difference between reconstructing all coincidences together (TSR) versus reconstructing trues (T) and scatter+randoms (SR) separately and then adding them. The difference maps and profiles indicate good agreement. Although voxel-level differences can reach up to 1%, no clear bias is observed, and at the volume-of-interest level these differences are even smaller.

Under the linearity assumption, the scatter- and random-corrected image was obtained by subtracting the SR-only reconstruction from the TSR reconstruction. The SR-only reconstruction was derived from a separate MC simulation. Figure B3 shows the scatter- and random-corrected reconstructed images of the XCAT phantom with inserted hot lesions. A comparison with Figure 9 (where only true coincidences are used) shows an expected decrease in the lesion CNR, as the SR correction method introduces additional noise. This effect is also apparent in the lesion profiles shown in Figure B4.

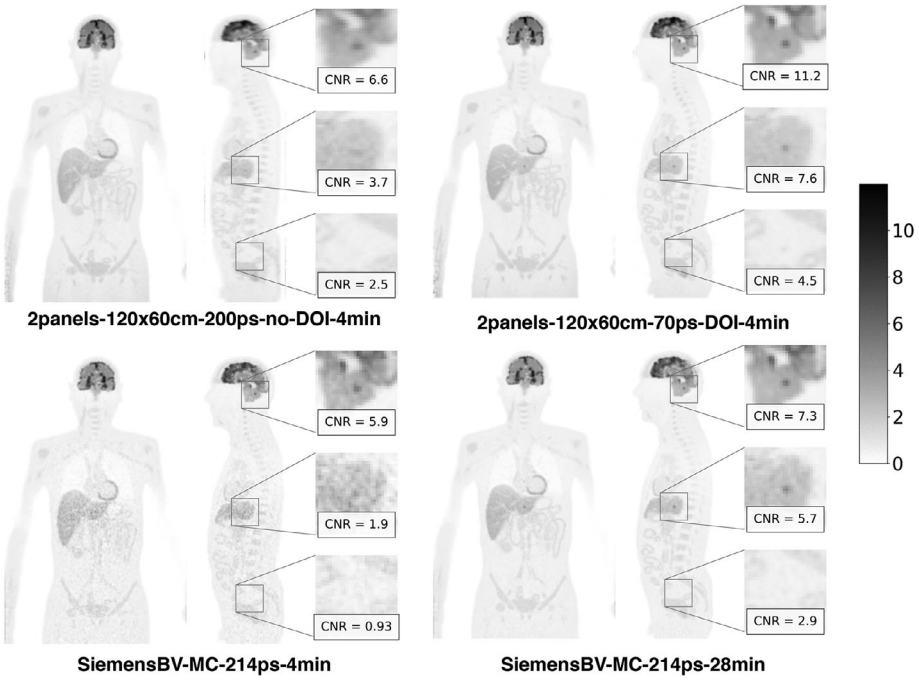

FIGURE B3 Reconstructed XCAT phantom images with scatter and random corrections applied, corresponding to the images in Figure 9 where only true coincidences were used.

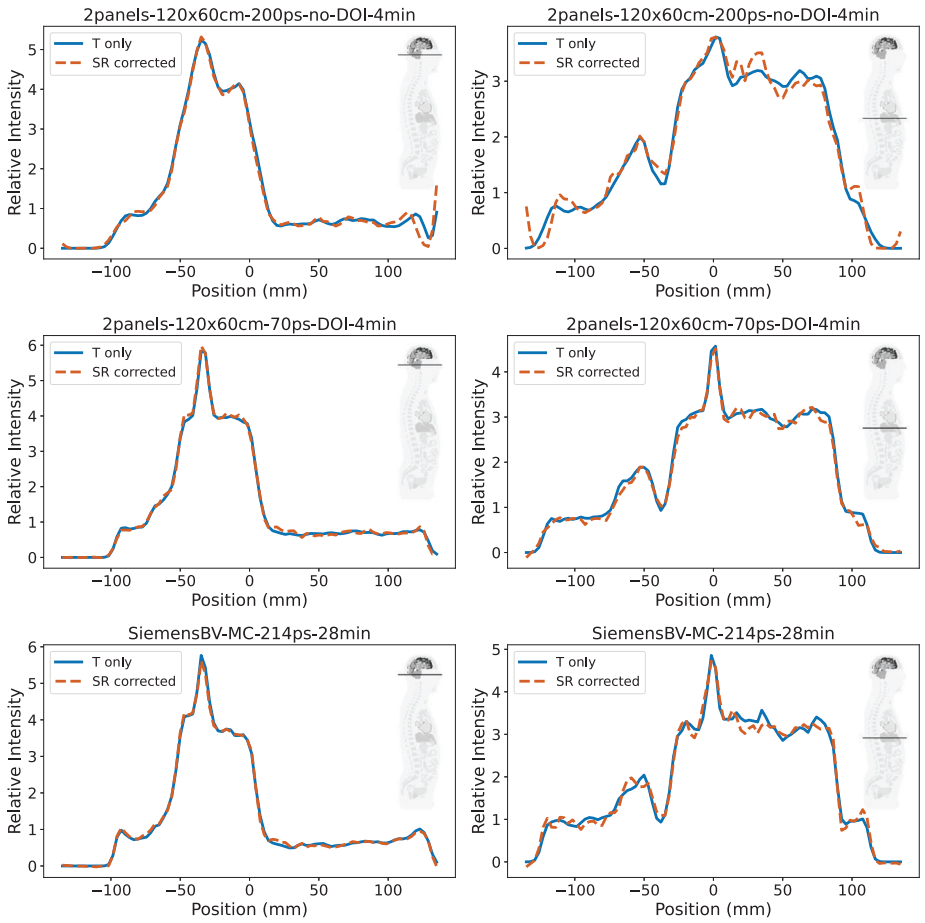

FIGURE B4 Profiles through the brain and liver lesions (indicated in the inset image) for reconstructions using only true coincidences, and for those corrected for scatter and random coincidences.